THE JOURNAL OF PHYSICAL CHEMISTRY B

Article

Cite This: J. Phys. Chem. B 2019, 123, 2094−2105

pubs.acs.org/JPCB

Imidazole and 1-Methylimidazole Hydrogen Bonding and Nonhydrogen Bonding Liquid Dynamics: Ultrafast IR Experiments

Jae Yoon Shin,[†] Yong-Lei Wang,[‡] Steven A. Yamada, Samantha T. Hung, and Michael D. Fayer*

Department of Chemistry, Stanford University, Stanford, California 94305, United States

Supporting Information

ABSTRACT: The dynamics of imidazole (IM) and 1-methylimidazole (1-MeIM) in the liquid phase at 95 °C were studied by IR polarization selective pump−probe and two-dimensional IR (2D IR) spectroscopies. The two molecules are very similar structurally except that IM can be simultaneously a hydrogen bond donor and acceptor and therefore forms extended hydrogen-bonded networks. The broader IR absorption spectrum and a shorter vibrational lifetime of the vibrational probe, selenocyanate anion ($SeCN^-$), in IM vs 1-MeIM indicate that stronger hydrogen bonding exists between $SeCN^-$ and IM. Molecular dynamics (MD) simulations support the strong hydrogen bond formation between $SeCN^-$ and IM via the HN moiety. $SeCN^-$ makes two H-bonds with IM; it is inserted in the IM H-bonded chains rather than being a chain terminator. The strong hydrogen bonding influenced the reorientation dynamics of $SeCN^-$ in IM, leading to a more restricted short time angular sampling (wobbling-in-a-cone). The complete orientational diffusion time in IM is 1.7 times slower than in 1-MeIM, but the slow down is less than expected, considering the 3-fold larger viscosity of IM. The jump reorientation mechanism accounts for the anomalously fast orientational relaxation in IM, and the MD simulations determined the average jump angle of the probe between hydrogen bonding sites. Spectral diffusion time constants obtained from the 2D IR experiments are only modestly slower in IM than in 1-MeIM in spite of the significant increase in viscosity. The results indicate that the spectral diffusion sensed by the $SeCN^-$ has IM hydrogen bond dynamics contributions not present in 1-MeIM.

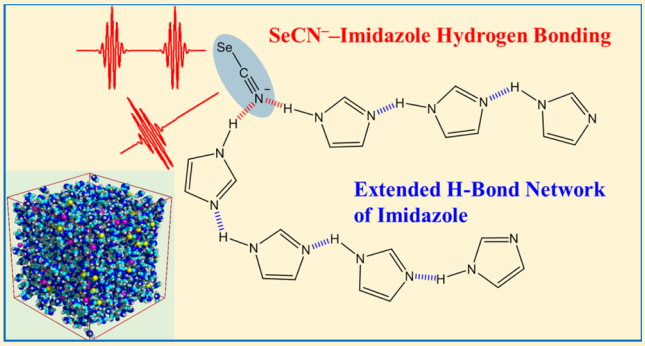

I. INTRODUCTION

Imidazole (IM) is a five-membered heterocyclic ring with two N atoms at the 1 and 3 positions, one of which (1 position) has an H atom covalently bound to it. This simple molecule is one of the principal components in nucleophilic and general base catalysts.[1] It is also the functional group of the amino acid histidine, the precursor to histamine that is commonly associated with the protein subunits that participate in proton transfer processes.[2−5]

IM, like alcohols and water, can act as both an H-bond donor and accepter owing to its two N atoms, one with and one without an H atom. It can form long hydrogen-bonded chains through these sites, as observed in pure IM crystals.[6,7] This is known to be responsible for IM's high proton conductivity, which is comparable to that of water.[8] Therefore, the local structure and hydrogen bond character of the pure IM system have been of considerable interest for understanding its proton transport mechanism.[9−16] It was proposed that the proton transport in pure IM occurs through the Grotthuss-type proton diffusion and reorientation of the IM ring,[9−11,17] i.e., proton shuttling in the hydrogen bond network followed by the reorganization of hydrogen bonds via rotation of the IM molecule. The dynamics of IM and its hydrogen bonding network play a central role in the proton transport in pure IM. Most of the experimental studies done on the pure IM system have used linear vibrational spectroscopy,[18−21] X-ray and neutron diffraction methods,[6,7,22] and solid state NMR.[23−25] However, the hydrogen bond dynamics and reorientation of small molecules usually happen on very fast time scales, on the order of picoseconds; direct observation of dynamics on the relevant time scale is beyond the ability of these experimental methods.

In this study, the dynamics of IM liquid were investigated with ultrafast vibrational spectroscopies, IR polarization selective pump−probe (PSPP) and two-dimensional IR (2D IR) techniques, along with molecular dynamics (MD) simulations. The effects of hydrogen bonding on the IM's dynamics were elucidated by comparing the results to those of 1-methylimidazole (1-MeIM), a simple IM derivative that cannot donate a hydrogen bond. Figure 1 shows the structures of 1-MeIM and IM. Because the pure IM is solid at room temperature and has a melting point of ∼90 °C, both 1-MeIM and IM were heated to 95 °C, slightly above the melting point of IM, to make valid comparisons of their liquid dynamics. The

Received: November 21, 2018
Revised: January 22, 2019
Published: February 6, 2019

DOI: 10.1021/acs.jpcb.8b11299
J. Phys. Chem. B 2019, 123, 2094−2105

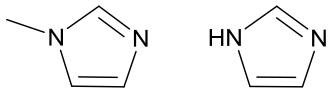

1-Methylimidazole (1-MeIM) Imidazole (IM)

Figure 1. Molecular structures of 1-methylimidazole (1-MeIM, left) and imidazole (IM, right).

CN stretch of the vibrational probe molecule, selenocyanate anion ($SeCN^-$), was used for the measurements; $SeCN^-$ is a useful probe that has been employed in studies of other systems,[26,27] including hydrogen bond dynamics of water.[28,29]

Relative to 1-MeIM, a broader CN stretch absorption band and shorter CN vibrational lifetime were observed in IM. These features indicate strong hydrogen bond formation between $SeCN^-$ and IM. The radial distribution function (RDF) from MD simulations also supports the formation of strong hydrogen bonds between $SeCN^-$ and the HN site of IM. This hydrogen bonding interaction affects the orientational relaxation of $SeCN^-$ measured with PSPP experiments, leading to more restricted wobbling-in-a-cone motions followed by jump reorientation. Finally, the three spectral diffusion time constants observed in the 2D IR experiments were only somewhat slower in IM than in 1-MeIM. The spectral diffusion of $SeCN^-$ in IM is influenced by H-bonding dynamics of the extended H-bond network of IM. The results provide a detailed picture of the liquid dynamics of IM, which play a fundamental role in proton transport.

II. EXPERIMENTAL AND THEORETICAL METHODS

II.I. Sample Preparation and Linear IR Spectroscopy. Potassium selenocyanate (99% purity) was purchased from Fisher Scientific (Acros Organics brand) and dried under vacuum (~100 mTorr) at 60 °C for 1 week. 1-Methylimidazole (≥99%, purified by redistillation), imidazole (≥99%, anhydrous), and deuterated imidazole (imidazole-d_4, 98 atom % D) were purchased from Sigma-Aldrich and used as received. All of the chemicals were stored in a nitrogen glovebox to prevent contamination from water and oxygen. To prepare the $SeCN^-$ sample, KSeCN was dissolved in 1-MeIM and IM at a molar ratio of 1:100 ion pairs to solvent molecules. Since imidazole is solid at room temperature, KSeCN and imidazole were mixed in solid state, and the mixture was melted at 95 °C to dissolve the KSeCN. Samples were sandwiched between two 3 mm thick, 1 in. diameter CaF_2 windows separated by a 56 μm poly(tetrafluoroethylene) ring spacer. For the imidazole sample, the solid mixture was sandwiched between the windows and melted on a hot plate. The sample preparation and sample cell assembly were conducted in a glovebox to prevent contamination. A cartridge heater connected to a variable alternating current voltage controller was used to heat the sample cell and to maintain the sample temperature at 95 °C for the high-temperature experiments. The room-temperature experiments were performed at 21.6 °C without heating. Linear IR spectra were recorded using a Thermo Scientific Nicolet 6700 Fourier transform infrared (FT-IR) spectrometer, which was purged with CO_2 and H_2O free air. The absorption spectrum of the pure solvent was subtracted from the spectrum of the probe containing samples to obtain the absorption spectrum of the CN stretch of $SeCN^-$.

II.II. Time-Resolved Ultrafast Infrared Experiments. The details of the experimental set-up have been described previously.[30] Briefly, a Ti:Sapphire regenerative amplifier pumped a home-built optical parametric amplifier for difference frequency generation, resulting in mid-IR pulses centered at 2065 cm^{-1} with ~6 μJ pulse energy. The mid-IR beam was split into two beams, a stronger pump pulse and weaker probe pulse. The pump pulse was passed through an acousto-optic mid-IR Fourier-domain pulse shaper. In the PSPP experiments, the pulse shaper chopped the pump pulse to obtain transient absorption signals, whereas in the 2D IR experiments, the pulse shaper generated two excitation pulses and controlled the delay time (τ) between them. In addition, the pulse shaper controlled the phases of the pulses, and a four-shot phase cycle was used to overcome light scattering.[30] A mechanical delay stage in the probe pulse path controlled the time delay between the pump and probe pulses in the PSPP experiments or the time delay (waiting time, T_w) between the second excitation pulse and the third excitation pulse (probe pulse) in the 2D IR experiments. The pulses were focused into the sample with a small crossing angle for both experiments.

After passing through the sample, the probe pulse was directed into a spectrograph. The spectrograph dispersed the probe pulse, which was then detected in the frequency domain by a 32-pixel HgCdTe (MCT) IR array detector. The 2D IR signal is collinear with the third pulse (probe pulse), which also acts as the local oscillator for heterodyne detection of the signal. For both PSPP and 2D IR measurements, the probe polarization was set to horizontal (in the plane of the optical table), and the pump polarization (both the first and second pump polarizations in the 2D IR experiments) was set to 45° with respect to the probe pulse. After the sample, a polarizer mounted in a computer-controlled rotation stage alternately resolved the probe pulse at +45° (parallel to the pump) and −45° (perpendicular to the pump) relative to the incident polarization (horizontal). In the 2D IR experiments, the two polarization configurations are noted as $\langle XXXX \rangle$ (parallel) and $\langle XXYY \rangle$ (perpendicular). Since the response of the spectrograph grating is polarization-dependent, another horizontal polarizer was placed in front of the spectrograph's entrance slit to ensure that there is no bias in the detection of the polarizations.

II.III. Ionic Models and Computations. Quantum chemical calculations were performed to optimize molecular geometries of 1-MeIM and IM molecules using the Gaussian 09 package[31] at B3LYP/6-311+G(d,p) level of theory with the inclusion of Grimme dispersion corrections. Harmonic frequency analysis was further performed to verify that the optimized molecular structures were at the global minima in the corresponding energy landscapes. Atomistic force field parameters for l-MeIM and IM molecules were developed based on the AMBER framework using the procedure described previously.[32,33] The CHELPG atomic partial charges on 1-MeIM and IM molecules were calculated at the same level of theory (the B3LYP hybrid functional and the 6-311+G(d,p) basis set). The force field parameters for K^+ and $SeCN^-$ were obtained from AMBER force field and work of Dhungana et al.,[34] respectively. The cross-interaction parameters between different atom types were obtained from the Lorentz−Berthelot combination rules.

Each simulation consists of 2000 1-MeIM (or IM) molecules and 50 KSeCN ion pairs. Atomistic simulations were performed using the GROMACS package with cubic

DOI: 10.1021/acs.jpcb.8b11299
J. Phys. Chem. B 2019, 123, 2094−2105

periodic boundary conditions.[35] The equations for the motion of all atoms were integrated using a classic Verlet leapfrog integration algorithm with a time step of 1.0 fs. A cutoff radius of 1.6 nm was set for short-range van der Waals interactions and real-space electrostatic interactions. The particle-mesh Ewald summation method with an interpolation order of 5 and Fourier grid spacing of 0.20 nm was employed to handle long-range electrostatic interactions in reciprocal space. All systems were energetically minimized using a steepest descent algorithm and annealed gradually from 800 to 370 K within 15 ns. The 1-MeIM/KSeCN system was further annealed to 300 K within 10 ns. The annealed systems were equilibrated in an isothermal−isobaric ensemble for 40 ns under controlled temperature and pressure (1 atm) by the Nosé−Hoover thermostat and the Parrinello−Rahman barostat with time coupling constants of 400 and 200 fs, respectively. Canonical ensemble simulations were executed for all systems up to 100 ns. Corresponding simulation trajectories were recorded with 100 fs intervals to analyze microstructures and dynamics.

III. RESULTS AND DISCUSSION

III.I. Linear IR Absorption Spectra. Figure 2A shows the FT-IR spectra of $SeCN^-$ in 1-MeIM and IM. The CN

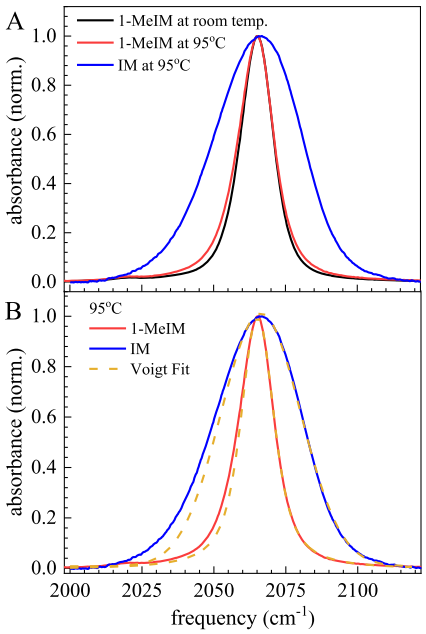

Figure 2. Background-subtracted FT-IR spectra of (A) $SeCN^-$ in 1-MeIM and IM at room temperature and 95 °C and (B) spectra with Voigt fits.

stretching band of $SeCN^-$ appears at 2065.2 cm^{-1} with a full width at half-maximum (FWHM) of 13.5 cm^{-1} in 1-MeIM at room temperature. At 95 °C, the band slightly broadens without a peak shift, with a FWHM of 14.4 cm^{-1}. In IM at 95 °C, however, the center frequency slightly shifts to the blue (higher frequency), 2066.3 cm^{-1}, with a much broader FWHM of 35.2 cm^{-1}. The blue shift of the center frequency accompanying the band broadening is indicative of a change in intermolecular interactions such as hydrogen bonding. The CN stretch with stronger hydrogen bonding is shifted to the blue in contrast to the OH or OD bands of HOD in D_2O and H_2O, respectively, which shift to lower frequencies with stronger hydrogen bonding.[29]

CN^-, which has a pure triple bond, absorbs well to the blue of $SeCN^-$, and has a much smaller transition dipole. The blue shift of the CN of $SeCN^-$ with stronger H-bonding can be qualitatively understood in terms of changes in the contributions of two $SeCN^-$ resonance structures, $[Se{-}C{\equiv}N]^-$ and $[Se{=}C{=}N]^-$. When the lone pair of the nitrogen atom in $SeCN^-$ forms a hydrogen bond, electron density shifts to the nitrogen atom, inducing more contribution from the $[Se{-}C{\equiv}N]^-$ resonance structure, which absorbs at a higher frequency (more like CN^-).[29] Stronger hydrogen bonds will increase the contribution from this resonance structure. Recent simulations of $SeCN^-$ in D_2O also found that a strong, axial hydrogen bond, in which the hydrogen donor points nearly parallel to the $SeCN^-$ axis, causes frequency blue shifts within the CN band.[28] Thus, the small blue shift and larger line width observed in IM indicate hydrogen bonding of $SeCN^-$ to IM. The variation in the hydrogen bond strengths results in an increased inhomogeneity of the absorption band relative to that of $SeCN^-$ in 1-MeIM.

Fitting Voigt line shape functions to the blue side of the peaks and extending the fits to the entire absorption bands revealed the asymmetry of the $SeCN^-$ band, especially in IM at 95 °C, as displayed in Figure 2B. The experimental absorption bands exhibit more absorption on the red side, deviating from the Voigt fit. A similar red wing has been observed for $SeCN^-$ in bulk D_2O where $SeCN^-$ forms hydrogen bonds to water.[28,29] The broadening on the red side of the line is attributed to the non-Condon effect (frequency-dependent transition dipoles). Weaker hydrogen bonds reduce the $[Se{-}C{\equiv}N]^-$ contribution and shift the spectrum to the red. Therefore, the red side of the $SeCN^-$ absorption line has a larger transition dipoles than the blue side because of the reduced contribution of $[Se{-}C{\equiv}N]^-$, i.e., less CN^- character.[28,29] The asymmetry of the $SeCN^-$ band in IM is ascribed to this non-Condon effect. On the other hand, the spectrum of $SeCN^-$ in 1-MeIM is almost symmetric, indicating less non-Condon effect and weaker H-bonds. As shown below by the MD simulations, there are a small number of very weak H-bonds between $SeCN^-$ and the H on the ring carbon between the two nitrogens of 1-MeIM. In contrast, $SeCN^-$ makes a large number of strong H-bonds of varying strengths to the HN of IM.

III.II. PSPP Measurements: Population Decay and Orientational Relaxation. In the PSPP experiments, the probe signals are polarization-resolved parallel ($S_{\parallel}$) and perpendicular ($S_{\perp}$) to the pump polarization and can be expressed as[36,37]

$$S_{\parallel}(t) = P(t)[1 + 0.8C_2(t)] \quad (1)$$

$$S_{\perp}(t) = P(t)[1 - 0.4C_2(t)] \quad (2)$$

where $P(t)$ is the isotropic pump−probe decay, i.e., population decay (vibrational lifetime), and $C_2(t)$ is the second-order Legendre polynomial orientational correlation function of the transition dipole moment given by[38]

$$C_2(t) = \langle P_2[\hat{\mu}(t)\cdot\hat{\mu}(0)]\rangle \quad (3)$$

with the second-order Legendre polynomial, P_2, and the transition dipole moment unit vector at time t, $\hat{\mu}(t)$. $\langle\cdots\rangle$ represents an ensemble average. The population decay is obtained from the combination of eqs 1 and 2 as

$$P(t) = [S_{\parallel}(t) + 2S_{\perp}(t)]/3 \quad (4)$$

DOI: 10.1021/acs.jpcb.8b11299
J. Phys. Chem. B 2019, 123, 2094−2105

Figure 3 shows the population decay data (points) of the CN stretch of $SeCN^-$ in 1-MeIM and IM at the center frequency of

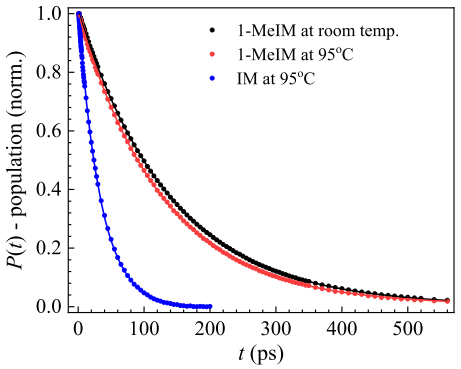

Figure 3. Population decay data (points) of 1-MeIM (room temperature and 95 °C) and IM (95 °C). Solid curves are single exponential fits to the data.

the absorption band. The population decay curves were fit with single exponential functions (solid curves), and the time constants were essentially the same across the inhomogeneously broadened absorption band for each sample, indicating a single ensemble of $SeCN^-$. The population decay time constants in 1-MeIM are 140.4 ± 0.6 ps at room temperature and 128.6 ± 0.5 ps at 95 °C. An increase in temperature can accelerate the vibrational energy relaxation by, e.g., increasing the occupation numbers of bath modes that can accept the vibrational energy.[39] In contrast to 1-MeIM, the vibrational lifetime in IM at 95 °C is much shorter, having a time constant of 33.5 ± 0.2 ps. This reduction in the lifetime is caused by the H-bonding of the $SeCN^-$ to the HN of IM because the H-bond interaction enhances coupling between the initially excited mode and modes of the solvent. For example, $SeCN^-$ in D_2O forms a strong H-bond and has a lifetime of 36.2 ps.[28] However, $SeCN^-$ has a lifetime of 105 ps in the room-temperature ionic liquid, 1-ethyl-3-methylimidazolium bis-(trifluoromethylsulfonyl)-imide ($EmimNTf_2$),[40] where $SeCN^-$ makes a very weak H-bond to the NTf_2^- anion. The vibrational lifetime becomes shorter in deuterated IM at 95 °C, with the time constant being 26.1 ± 0.1 ps (see Figure S1 in the Supporting Information). The DN stretch is closer in frequency to the CN stretch than the HN stretch, providing a more efficient pathway for vibrational relaxation via the H-bond coupling.

The anisotropy decay also can be calculated from PSPP experiments to obtain the orientational dynamics of $SeCN^-$, i.e., orientational correlation function, $C_2(t)$

$$r(t) = \frac{S_{\parallel}(t) - S_{\perp}(t)}{S_{\parallel}(t) + 2S_{\perp}(t)} = 0.4C_2(t) \tag{5}$$

The anisotropy is the orientational correlation function scaled by 0.4. However, inertial motion occurs on a faster time scale than the temporal resolution of the instrument, which results in an initial value below 0.4 when $r(t)$ is extrapolated to $t = 0$. Figure 4 displays the anisotropy experimental decays (points) measured in 1-MeIM and IM. In 1-MeIM, the anisotropy decays more quickly at a higher temperature, 95 °C, than at room temperature. The anisotropy decay in IM is slower than that of 1-MeIM sample at 95 °C. Triexponential functions give the best fits (solid curves in Figure 4) to the data for all of the

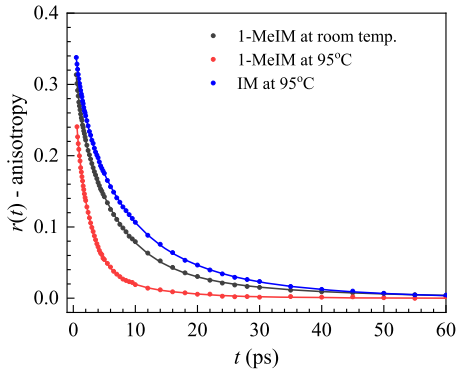

Figure 4. Anisotropy decay data (points) of 1-MeIM (room temperature and 95 °C) and IM (95 °C). Solid curves are triexponential fits to the data. The fit parameters are given in Table 1.

samples (see Figure S2 in the Supporting Information for details of the fitting procedures). The fit parameters are tabulated in Table 1.

If the orientational relaxation undergoes free diffusion for complete randomization, the orientational correlation function is a single exponential function given by

$$C_2(t) = \exp[-6D_m t] \tag{6}$$

where D_m is the orientational diffusion constant. However, the anisotropy decays of $SeCN^-$ in 1-MeIM and IM are triexponentials. The vibrational lifetime measurements confirmed a single ensemble of $SeCN^-$, ruling out the possibility that the triexponential anisotropy decay arises from three subensembles undergoing orientational relaxation with distinct diffusion time constants. Instead, the multiexponential behavior of the anisotropy can be interpreted as restricted angular motions followed by a complete orientational randomization, i.e., wobbling-in-a-cone.[41−43] In this model, the angular space that the transition dipole explores during the restricted orientational diffusion is quantified by a cone of half angle, θ_c, and the orientational correlation function decays to a plateau in the absence of further orientational relaxation. The plateau amplitude is the square of the generalized order parameter, Q^2.

$$C_2(t) = Q^2 + (1 - Q^2)\exp[-t/\tau_c] \tag{7}$$

$$Q^2 = \left[\frac{1}{2}\cos\theta_c(1 + \cos\theta_c)\right]^2 \tag{8}$$

where τ_c is the correlation time for restricted angular diffusion. On a slower time scale, the orientational correlation function decays to zero due to the complete reorientation through the unrestricted free diffusion. Thus, based on the experimental deviation from 0.4 at $t = 0$ and the triexponential decay of the anisotropy, the wobbling model must include an inertial cone, two diffusive cones, and the complete reorientation, accounting for the ultrafast inertial motion, the short and intermediate exponential decays, and the longest exponential decay that takes the anisotropy to zero. The resulting orientational correlation function is[44]

$$C_2(t) = T^2(S^2 + (1 - S^2)\exp[-t/\tau_{c1}])(R^2 + (1 - R^2)\exp[-t/\tau_{c2}])\exp[-t/\tau_m] \tag{9}$$

where T, S, and R are the generalized order parameters for the inertial, first diffusive, and second diffusive cones, respectively. τ_{c1}, τ_{c2}, and τ_m are the correlation times for the first and second

DOI: 10.1021/acs.jpcb.8b11299
J. Phys. Chem. B 2019, 123, 2094−2105

Table 1. Parameters from the Triexponential Fits to the Anisotropy Decays

sample		A_1[a]	t_1 (ps)	A_2[a]	t_2 (ps)	A_3[a]	t_3 (ps)
1-MeIM	RT	0.09 ± 0.01	0.9 ± 0.1	0.23 ± 0.01	6.2 ± 0.2	0.05 ± 0.01	24.1 ± 2.0
	95 °C	0.08 ± 0.03	0.3 ± 0.1	0.24 ± 0.01	2.3 ± 0.1	0.05 ± 0.01	9.7 ± 0.8
IM	95 °C	0.08 ± 0.01	1.3 ± 0.1	0.17 ± 0.02	6.3 ± 0.6	0.13 ± 0.02	16.8 ± 1.1

[a] A_i is the amplitude of each exponential.

Table 2. Parameters from Wobbling Analysis

sample		θ_{in} (deg)[a]	θ_{c1} (deg)[b]	θ_{c2} (deg)[b]	θ_{tot} (deg)[c]	τ_{c1} (ps)[d]	τ_{c2} (ps)[d]	τ_m (ps)[d]	D_{c1} (10^{-2} ps^{-1})[e]	D_{c2} (10^{-2} ps^{-1})[e]
1-MeIM	RT	14 ± 2	24 ± 1	58 ± 1	62 ± 1	0.9 ± 0.1	8.4 ± 0.4	24 ± 2	5.4 ± 0.4	2.4 ± 0.2
	95 °C	14 ± 5	23 ± 3	58 ± 1	63 ± 1	0.3 ± 0.1	3.1 ± 0.1	10 ± 1	13 ± 5	6.8 ± 0.6
IM	95 °C	11 ± 8	22 ± 1	42 ± 3	47 ± 3	1.3 ± 0.1	10 ± 2	17 ± 1	3.2 ± 0.5	1.3 ± 0.3

[a] The inertial cone angle. [b] θ_{c1} and θ_{c2} are the first and second diffusive cone half angles. [c] The total cone half angle accounting for all three cones. [d] τ_{c1}, τ_{c2}, and τ_m are the decay times associated with the first and second diffusive cones and the final free diffusion, respectively. [e] D_{c1} and D_{c2} are the first and second cone diffusion constants.

diffusive cones and the free diffusion time for the complete orientational randomization. Since the inertial motion is too fast to be observed (i.e., $\tau_{in} \sim 0$), only the order parameter for the inertial cone, T, appears. From eq 6 and the last exponential term of eq 9, the orientational diffusion constant is $D_m = 1/6\tau_m$. The orientational diffusion constants for the wobbling motion are obtained from the half angles, order parameters, and correlation times.[42,45] The amplitudes and time constants of the triexponential fit to the anisotropy, which are given in Table 1, were used to calculate the half angles, order parameters, and correlation times in the wobbling model.[44]

The resulting parameters from a wobbling-in-a-cone analysis are summarized in Table 2. In 1-MeIM, the half angles of the inertial and restricted diffusive cones do not change with temperature, whereas the time constants for the first and second diffusive cones significantly decrease at 95 °C compared to room temperature. This leads to an increase in the orientational wobbling diffusion constants, D_{c1} and D_{c2}. The restricted angular sampling of $SeCN^-$ originates from structural constraints imposed by surrounding molecules. As the liquid structure fluctuates, these constraints relax to allow increased angular sampling. In 1-MeIM, the increase in the wobbling diffusion constants with increased temperature reflects a more rapid sampling of the same angular range, which is caused by an increased thermal energy accelerating the structural fluctuations that lead to a more rapid relaxation of structural constraints.

Comparing 1-MeIM and IM at 95 °C, the half angle for the second diffusive cone of IM is noticeably smaller than that of 1-MeIM, whereas the other two half angles, θ_{in} and θ_{c1}, are the same in the two solvents. Overall, the total half angle, θ_{tot}, becomes smaller in IM. In addition, the correlation times for both the first and the second diffusive cones are slower in IM. The net result of differences in the half angles and correlation times produces the reduced wobbling diffusion constants in IM. Since the molecular structures of 1-MeIM and IM are very similar, the slowdown in the wobbling rates and more restricted half angles in IM can be attributed to stronger intermolecular interactions, i.e., hydrogen bonding. The strong hydrogen bonding of $SeCN^-$ with IM molecules is likely to impede the wobbling motion and limit its angular range. The same trend is observed in the complete orientational diffusion time, τ_m: it is shorter in 1-MeIM at high temperature than at room temperature and is longer in IM compared to 1-MeIM at the same temperature (see Table 2). Frequently, the complete orientational relaxation time can be related to the viscosity via the Stokes Einstein Debye equation[46,47]

$$\tau_m = \frac{\eta(T)V\lambda}{k_B T} \tag{10}$$

where k_B is the Boltzmann constant, T is the absolute temperature, η is the dynamic viscosity, V is the volume of the molecule, and λ is a friction coefficient that can be determined from the boundary conditions and molecular shape of the rotator.[48] Thus, if the rotator's properties and the boundary conditions do not change, the orientational relaxation time only depends on the bulk viscosity and temperature. τ_m in the 1-MeIM sample decreases at 95 °C by a factor of 2.4 compared to the room-temperature value. The viscosities of 1-MeIM were measured to be 1.72 and 0.73 cP at 25 and 95 °C, respectively (see the Supporting Information). The combination of changes in viscosity and temperature gives a 2.9-fold decrease based on eq 10, which is reasonably close to the measured ratio, and just within the error bars of the measurements of τ_m at the two temperatures.

The orientational diffusion time, τ_m, of IM at 95 °C is 1.7-fold longer than that of 1-MeIM measured at the same temperature. The viscosity of IM at 95 °C is 2.28 cP, which is larger than 1-MeIM's viscosity at the same temperature by a factor of 3.1 (see the Supporting Information). The increase in viscosity of IM is substantially larger than the increase in τ_m: the measured orientational time constant is almost twice as fast in IM as would be expected from the viscosity change alone. A different mechanism for the orientational relaxation occurs in IM as discussed in Section III.V.I.

III.III. Two-Dimensional (2D) IR Measurements: Spectral Diffusion. Two-dimensional (2D) IR spectroscopy can quantitatively measure spectral diffusion. The measurements provide the amplitudes and time scales of the solvent's frequency fluctuations that cause the loss of correlation between the initial and final oscillator frequencies within an inhomogeneously broadened absorption line. The inhomogeneous line is a result of local and mesoscopic solvent structures that determine a vibrational chromophore's frequency in the inhomogeneous line through intermolecular interactions. As the solvent structure evolves in time, the intermolecular interactions with the vibrational probe change. The time-dependent intermolecular interactions cause the vibrational frequencies to be time-dependent. Therefore, measuring the

DOI: 10.1021/acs.jpcb.8b11299
J. Phys. Chem. B 2019, 123, 2094−2105

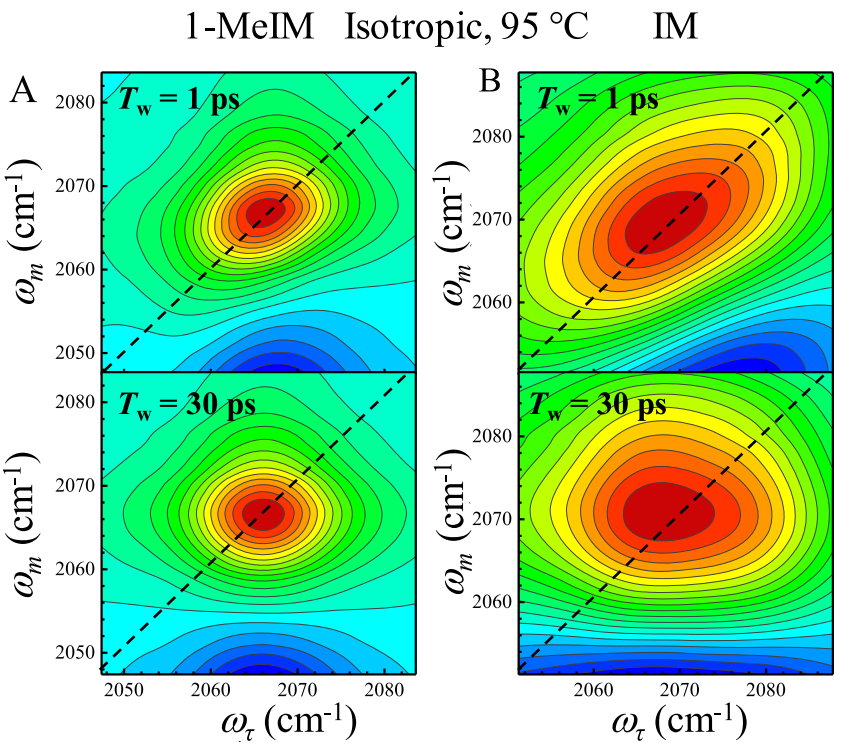

Figure 5. Isotropic 2D IR spectra of (A) 1-MeIM and (B) IM at T_w = 1 ps (top panels) and T_w = 30 ps (bottom panels) measured at 95 °C. Dashed lines are the diagonals.

time evolution of the vibrational probes' frequencies reports on the time dependence of the solvent structure.

A series of 2D spectra were acquired at different waiting times, T_w, and the changes in the 2D spectral shapes were quantified by the center line slope (CLS) method. The CLS decay as a function of T_w gives the time-dependent normalized frequency−frequency correlation function (FFCF).[35,49,50] The FFCF is the joint probability that an oscillator with an initial frequency will have the same frequency at a time t later, averaged over all initial frequencies in the inhomogeneous spectral distribution. The FFCF was modeled with a multiexponential form

$$C(t) = \langle \delta\omega(t)\delta\omega(0)\rangle = \sum_i \Delta_i^2 \exp(-t/\tau_i) \tag{11}$$

where Δ_i and τ_i are the frequency fluctuation amplitude and associated time constant, respectively, for the ith component. $\delta\omega(t) = \omega(t) - \langle\omega\rangle$ is the instantaneous frequency fluctuation, where $\langle\omega\rangle$ is the average frequency. A component of the FFCF is motionally narrowed and contributes to the homogeneously broadened absorption line if $\Delta\tau \ll 1$. In this case, Δ and τ cannot be determined separately. The motionally narrowed contribution has a pure dephasing line width given by $\Gamma^* = \Delta^2\tau/\pi = 1/\pi T_2^*$, where T_2^* is the pure dephasing time. The observed homogeneous dephasing time, T_2, also depends on the vibrational lifetime and the orientational relaxation

$$\frac{1}{T_2} = \frac{1}{T_2^*} + \frac{1}{2T_1} + \frac{1}{3T_{or}} \tag{12}$$

where T_1 and T_{or} are the vibrational lifetime and orientational relaxation time, respectively. The total dephasing time, T_2, and the absolute fluctuation amplitudes, Δ_i, are calculated by the simultaneous fit to the CLS decay and the linear absorption spectrum, constructing the complete FFCF of eq 11.[35,49,50]

Recently, it was found that in certain cases the rotation of the probe molecule contributes to the spectral diffusion, in addition to the structural fluctuations of the solvent, causing different CLS decays in $\langle XXXX\rangle$ (parallel) and $\langle XXYY\rangle$ (perpendicular) polarization configurations.[45,51] This phenomenon is referred to as reorientation-induced spectral diffusion (RISD), which, for a molecule with a permanent dipole moment, is caused by the first-order Stark effect.[45,51,52] The RISD effect becomes prominent when the electric field from the surrounding environment varies on a time scale similar to the orientational relaxation time of the probe molecule. In this study, we observed only small differences in the CLS curves between parallel and perpendicular polarization configurations for all samples, indicating that the RISD contribution to the spectral diffusion is very small (see the Supporting Information for the CLS curves measured with parallel and perpendicular polarizations). Thus, the isotropic 2D IR spectra were constructed from the parallel and perpendicular 2D IR spectra, $\langle XXXX\rangle + 2\langle XXYY\rangle$, and were used to analyze the spectral diffusions in the samples.

Figure 5 shows the isotropic 2D IR spectra of 1-MeIM and IM at T_w = 1 and 30 ps measured at 95 °C. The red bands with positive amplitude centered on the diagonal line arise from the 0−1 vibrational transitions. The off-diagonal partial blue bands beneath the 0−1 bands arise from the 1−2 transitions. Like the linear IR absorption spectra shown in Figure 2, $SeCN^-$ in IM shows a broad feature in the 2D IR spectrum compared to 1-MeIM. The elongated shape of the 2D IR spectrum at T_w = 1 ps changes to a rounder shape at T_w = 30 ps as the ensemble loses correlation between the initial and final frequencies. These 0−1 transition bands were used in the CLS analysis to obtain a quantitative measure of the spectral diffusion and the FFCF.

DOI: 10.1021/acs.jpcb.8b11299
J. Phys. Chem. B 2019, 123, 2094−2105

The isotropic CLS decays of 1-MeIM and IM are displayed in Figure 6. The CLS curves were fit with triexponential functions, and the resulting parameters were used to calculate FFCFs from eq 11 (see Figure S7 in the Supporting Information for details of the fitting). The homogeneous line width, frequency fluctuation amplitudes, and decay time constants for the FFCFs extracted from the isotropic CLS decays are given in Table 3.

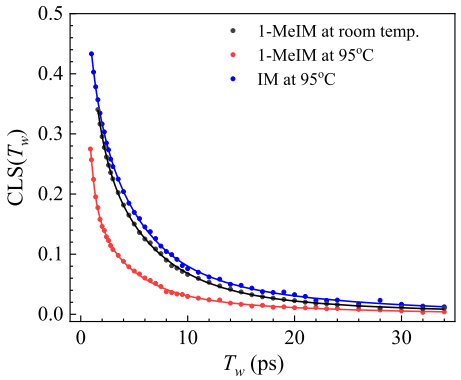

Figure 6. Isotropic CLS decay data (points) of 1-MeIM (room temperature and 95 °C) and IM (95 °C). Solid curves are triexponential fits to the data. The fit parameters were used to calculate the FFCFs. The FFCF parameters are given in Table 3.

As shown in Figure 6, the CLS curve of 1-MeIM decays faster at 95 °C than it does at room temperature. The decay time constants, τ_1, τ_2, and τ_3, of the FFCF at 95 °C are 80, 40, and 30% faster, respectively, than the room-temperature values, although the error bars for the τ_3 values slightly overlap. The decay time constants of the FFCF reflect the time scales of structural fluctuations of 1-MeIM that induce the spectral diffusion in the CN band of $SeCN^-$, which become faster at a higher temperature.

The CLS data for the IM sample exhibits a substantially slower decay than the 1-MeIM sample at the same temperature, 95 °C (Figure 6). The fast time constant, τ_1, is 60% slower in IM, whereas τ_2 is only 17% slower. The error bars for the time constants in the two liquids almost overlap. The slowest time constants, τ_3, are the same within error bars for the two liquids. In addition, the amplitude percentages of the processes in IM are larger for the slower components of the FFCF compared to 1-MeIM (see Table 3). H-bond interactions seem to slow down the spectral diffusion in IM.

III.IV. MD Simulations: Hydrogen Bonding Interactions in 1-MeIM and IM. To understand the different hydrogen bonding interactions in 1-MeIM and IM, MD simulations were performed as described in Section II.III. The 1-MeIM and IM molecules have three types of H atoms that have different capacities for hydrogen bonding interactions with the lone pair of the N atom of $SeCN^-$ (see the molecular structures in Figure 7). The RDFs between the N atom of $SeCN^-$ and the H atoms of the solvents were calculated at 370 K and are displayed in Figure 7. For 1-MeIM, the H5 atom (Figure 7A) can form a relatively weak hydrogen bond with the N atom of $SeCN^-$, leading to a non-negligible amplitude of the RDF near 0.25 nm radial distance. The H4 and HC atoms (Figure 7A), however, have essentially no tendency to form hydrogen bonds with $SeCN^-$ due to their lower electronegativities relative to the H5 atom of 1-MeIM.

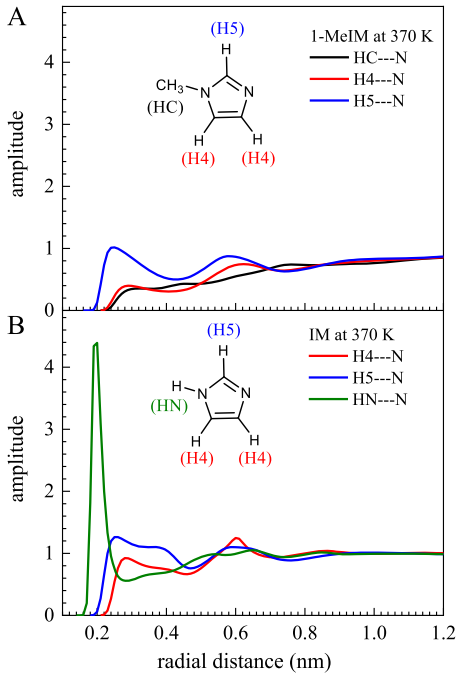

Figure 7. Radial distribution functions (RDFs) for the two simulated systems, (A) $SeCN^-$ in 1-MeIM and (B) $SeCN^-$ in IM, at 370 K. H atom positions are labeled in the molecular structures.

In contrast to 1-MeIM, the presence of an H atom bound to the N atom of IM (labeled as HN in Figure 7B) results in greatly increased hydrogen bonding. A sharp peak with a large amplitude appears in the RDF plot near 0.2 nm for the HN atom, and a broad band is observed near 0.25 nm for the H5 atom. For the H4 atom, the first band has less amplitude than the second band, indicating little likelihood of it forming a hydrogen bond with $SeCN^-$. These computational results demonstrate that both HN and H5 atoms in IM can participate in hydrogen bonding interactions with $SeCN^-$, and the HN atom forms a far stronger hydrogen bond with $SeCN^-$ than the other hydrogen bond types in the IM liquid. In addition, the simulations showed that the majority of $SeCN^-$ anions can form two hydrogen bonds with IM molecules via HN and/or H5 atoms. In the 1-MeIM liquid, $SeCN^-$ anions also can form two hydrogen bonds through the H5 atoms of 1-MeIM, but,

Table 3. Isotropic FFCF Parameters

sample		Γ (cm^{-1})[a]	Δ_1 (cm^{-1})[b]	τ_1 (ps)[c]	Δ_2 (cm^{-1})[b]	τ_2 (ps)[c]	Δ_3 (cm^{-1})[b]	τ_3 (ps)[c]
1-MeIM	R.T.	1.7 ± 0.2	4.6 ± 1.4 (45%)[d]	0.9 ± 0.2	4.1 ± 0.2 (40%)[d]	4.8 ± 0.5	1.6 ± 0.6 (16%)[d]	19 ± 4
	95 °C	1.7 ± 0.8	6.7 ± 1.2 (55%)[d]	0.5 ± 0.1	3.7 ± 0.2 (31%)[d]	3.5 ± 0.3	1.8 ± 0.3 (15%)[d]	15 ± 1
IM	95 °C	9.3 ± 3.0	8.2 ± 1.7 (36%)[d]	0.8 ± 0.2	9.7 ± 0.5 (42%)[d]	4.1 ± 0.3	4.9 ± 0.8 (21%)[d]	17 ± 2

[a]Γ: homogeneous line width (full width at half-maximum). [b]Δ_i: inhomogeneous line width (standard deviation) of the ith component. [c]τ_i: decay time constant of the ith component. [d]Amplitude percentage of the ith component: $100 \times \Delta_i/(\Delta_1 + \Delta_2 + \Delta_3)$.

DOI: 10.1021/acs.jpcb.8b11299
J. Phys. Chem. B 2019, 123, 2094−2105

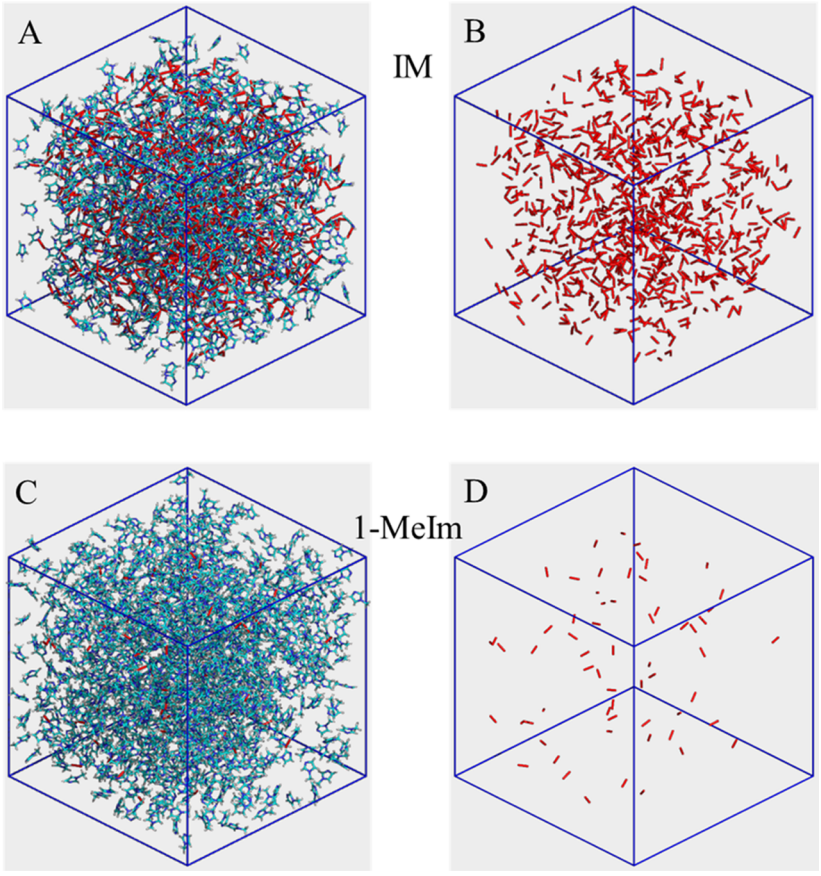

Figure 8. Simulated solvent structures and hydrogen bonds (red) of IM (top panels, A and B) and 1-MeIM (bottom panels, C and D) at 370 K. Right panels show a clear view of hydrogen bonds in (B) IM and (D) 1-MeIM by omitting the molecular structures. KSeCN is also omitted in the figures for clarity.

because such H-bonds are very weak, their probabilities of formation are much lower than the two H-bonds formation in IM. Therefore, a large variation is expected in hydrogen bond strengths of $SeCN^-$ in IM, which is consistent with its broad IR absorption band shown in Figure 2. Moreover, the strong hydrogen bond interaction between $SeCN^-$ and IM, formed at the HN position, is responsible for the blue shift, and the variation in the strengths of the strong H-bonds gives rise to the non-Condon effect observed in the IR absorption band of IM. In the 1-MeIM liquid, weak hydrogen bonding only to the H5 atom results in a less inhomogeneous broadening of the CN stretch and a narrower IR absorption band (see Figure 2).

Hydrogen bonds also form between IM molecules. In IM, there are two hydrogen bond donors (HN and H5 atoms as labeled in Figure 7B) and one hydrogen bond acceptor, the lone pair of the N. Therefore, IM can simultaneously act as a hydrogen bond donor and an acceptor. The N lone pair can accept an H-bond from either HN or H5 of another IM, and HN or H5 can donate an H-bond to the lone pair of another IM. Thus, IM molecules can form a hydrogen bonding network. This extended network of long hydrogen-bonded chains has been observed in X-ray crystal structures of IM crystals.[6,7] An extended hydrogen bond network is also present in the pure IM liquid, as revealed by these atomistic simulations. Figure 8 displays hydrogen bonding networks in IM and 1-MeIM from the simulations performed at 370 K. The left panels, Figures 8A,C, present the molecular configurations of IM and 1-MeIM with the hydrogen bonds shown in red. For a clearer view, only the red-colored hydrogen bonds are displayed in the right panels, Figures 8B,D, with molecular structures omitted. The simulations clearly show that most IM molecules are connected through hydrogen bonding to form an extended hydrogen bonding network, analogous to those formed by polyalcohols.[53,54] The major bonding configuration in IM is the hydrogen bond between the HN of one IM and the N lone pair of another IM. In contrast, 1-MeIMs form a small number of hydrogen bonds, lacking an extended network.

III.V. Hydrogen Bonding Dynamics in IM. *III.V.I. Orientational Relaxation: Jump Reorientation Mechanism.* The anomalously fast orientational relaxation in IM, which does not track the viscosity change, is interesting. One possibility is that $SeCN^-$ experiences a different hydrodynamic boundary condition in 1-MeIM and IM. Among two boundary conditions, stick boundary conditions apply when the reorienting solute is large or comparable in size to the solvent molecules. In contrast, slip boundary conditions generally apply when the rotating molecule is small compared to the surrounding solvent molecules. Friction arises from rotator's swept volume as solvent molecules need to move to allow reorientation of the solute. The orientational diffusion of $SeCN^-$ in room-temperature ionic liquids is an example where a slip boundary condition occurs.[55,56] Just considering the size of the $SeCN^-$ relative to the sizes of the molecular species, 1-MeIM and IM, one would expect stick boundary conditions in both liquids because the size of $SeCN^-$ is comparable to the size of both solvent molecules.

DOI: 10.1021/acs.jpcb.8b11299
J. Phys. Chem. B 2019, 123, 2094−2105

However, slip boundary conditions for $SeCN^-$ in IM might occur because of the extended H-bond network that exists in IM but does not occur in 1-MeIM, as shown in Figure 8. In effect, the $SeCN^-$ is small compared to the H-bonded network of IM solvent, possibly giving rise to slip boundary conditions. This behavior, i.e., a change in hydrodynamic boundary conditions, was previously reported for the orientational relaxation times of rhodamine B measured when the solvent was changed from *n*-alcohols to polyalcohols.[47] Specifically, the orientational relaxation times of rhodamine B displayed stick boundary conditions in *n*-alcohols like ethanol, propanol, heptanol, and decanol. In contrast, slip boundary conditions were observed in polyalcohols like ethylene glycol and ethylene glycol−glycerol mixtures. Polyalcohols have extended hydrogen bonding networks and act as "large" molecule solvents.[53,54] The extended hydrogen bond network in IM might result in slip boundary conditions in the same manner as found in polyalcohols.

For slip boundary conditions, in eq 10, the friction coefficient, λ, for spheroids can be calculated from the ratio of the minor axis to the major axis, ρ.[48] Modeling $SeCN^-$ as a prolate spheroid, the lengths of the major and minor axes are 3.3 and 2.2 Å, respectively, from geometry optimization calculations.[26] Then ρ = 0.6. From the tabulated values for prolate spheroids with ρ = 0.6, the ratio of the slip to stick friction coefficients is 0.144.[48] Then, taking into account the change in viscosity, for stick boundary conditions the final relaxation time constant, τ_m, of IM should be 3.1 times slower than 1-MeIM at 95 °C, and under slip boundary conditions it should be 0.45 time faster.

The fact that the orientational relaxation of $SeCN^-$ in IM is not well described by either limiting cases of stick or slip hydrodynamic boundary is not surprising. In contrast to 1-MeIM, in IM, $SeCN^-$ must break an H-bond to undergo orientational relaxation because it makes two H-bonds to the HN and H5 (see Figure 7B). The spectrum and the vibrational lifetime measurements showed that there is only one ensemble of $SeCN^-$'s, which is H-bonded. There is no indication of a significant population of free (not H-bonded) $SeCN^-$. Therefore, when $SeCN^-$ breaks an H-bond with one IM molecule, it will immediately form another H-bond with a different IM molecule. This reorientation mechanism is referred to as jump reorientation, which is the mechanism responsible for orientational relaxation in water.[57] It is different from the description of orientational relaxation embodied in eq 10 that is based on the small angular step Gaussian diffusion.

For jump reorientation, the observed rate of orientational relaxation is determined by the jump time and the jump angle. The relation is given by[57]

$$\tau_0 = \tau_m \frac{5\sin(\theta/2) - \sin(5\theta/2)}{5\sin(\theta/2)} \quad (13)$$

where τ_0 is the jump time and θ is the jump angle.

The MD simulations, in fact, demonstrate that $SeCN^-$ undergoes a jump orientation in IM. The simulations show that when an $SeCN^-$ breaks one of its H-bonds, it immediately forms another H-bond with a different H-bond acceptor, HN or H5, on a neighboring IM molecule. To determine the average jump angle, the distribution of the change in angle upon H-bond switching was evaluated. The average jump angle was calculated to be 73 ± 5° (as an aside, a 60° jump angle occurs in water[57]). Substituting τ_m = 17 ps and θ = 73° into eq 13 gives a jump time of 17 ps. For this particular θ, the jump time is the same as the measured orientational relaxation time constant.

III.V.II. Spectral Diffusion. The slower spectral diffusion in IM compared to 1-MeIM at 95 °C is almost certainly the result of the strong H-bonds and the extended H-bond network in IM, as shown in Figure 8. The IM H-bond networks result in IM being a solid at room temperature with a melting point of ∼90 °C, whereas 1-MeIM is a liquid at room temperature. At 95 °C, the viscosity of IM is 3.1 times that of 1-MeIM. Given these differences, it is notable that the spectral diffusion in IM is as fast as it is compared to 1-MeIM. However, the extended H-bond network and H-bond dynamics provide a source of structural fluctuation in IM, which will not exist to a significant extent in 1-MeIM (see Figure 8).

A recent study of water dynamics with the $SeCN^-$ anion probe demonstrated that the time scales of the spectral diffusion sensed by $SeCN^-$ in D_2O are consistent with those probed by the OH of HOD.[28] The two decay time constants of the spectral diffusion were measured to be 0.6 ± 0.1 and 1.4 ± 0.2 ps with $SeCN^-$ vs 0.4 ± 0.1 and 1.4 ± 0.2 ps with HOD in D_2O.[28,58] According to atomistic molecular simulations of pure water, the fast and slow components of the spectral diffusion correspond to local fluctuations in hydrogen bond geometries and large-scale rearrangement of the extended hydrogen bond network, respectively.[58,59] The study showed that $SeCN^-$ also reports on the water hydrogen bond dynamics via spectral diffusion, and the presence of the $SeCN^-$ anion does not largely alter the hydrogen bond dynamics of water.[28] IM and water are similar in the sense that they can form extended hydrogen bond networks and H-bond to $SeCN^-$ through good H-bond donors, NH and OH. Therefore, it is likely that the spectral diffusion sensed by $SeCN^-$ in IM arises from the H-bond dynamics of IM. Then, the origins of spectral diffusion in 1-MeIM and IM are substantially different.

IV. CONCLUDING REMARKS

In this study, the liquid dynamics of IM at 95 °C was investigated by PSPP and 2D IR spectroscopies with the use of $SeCN^-$ as a vibrational probe. The IM dynamics were compared to those of 1-MeIM, the simplest derivative of IM. Although IM is an H-bond donor and acceptor, 1-MeIM is only an acceptor. This difference has a significant impact on the nature of the two liquids.

The FT-IR spectra at 95 °C showed that the CN stretch band of $SeCN^-$ in IM is only slightly blue shifted compared to 1-MeIM (2066.3 vs 2065.2 cm^{-1}) but has a substantially wider line width (35.2 vs 14.4 cm^{-1}). In addition, the IM band has a large red wing caused by the non-Condon effect.[28,29] These features of the $SeCN^-$ in IM are indicative of substantial H-bonding to the N lone pair not present in 1-MeIM (Figure 7). The RDF calculations (Figure 7) corroborated the strong hydrogen bond formation of $SeCN^-$ to IM through the HN position. In addition, it was found that $SeCN^-$ can form two hydrogen bonds to IM via two H atom positions, HN and H5, although the H-bond to HN is much stronger. The wide range of H-bond configurations and strengths gives rise to the broad bandwidth of the CN stretch absorption spectrum in IM. $SeCN^-$ can also make hydrogen bonds to 1-MeIM, but they are very weak and only through the H5 position. In the simulated solvent structures (Figure 8), most IM molecules were connected through hydrogen bonding, establishing an extended hydrogen bond network, whereas only a smaller

DOI: 10.1021/acs.jpcb.8b11299
J. Phys. Chem. B 2019, 123, 2094−2105

number of hydrogen bonds with no extended network were observed in 1-MeIM.

The PSPP experiments measured the vibrational lifetime and orientational anisotropy decay. The vibrational lifetime of the $SeCN^-$'s CN stretch in IM is 33.5 ± 0.2 ps, much shorter than that in 1-MeIM, 128.6 ± 0.5 ps at 95 °C. This is another result of strong H-bonding in IM, which facilitates the vibrational relaxation. The complete orientational diffusion time of $SeCN^-$ slowed down in IM by a factor of 1.7 compared to that in 1-MeIM. However, a 3.1-fold larger viscosity of IM than 1-MeIM suggested that the orientational diffusion of $SeCN^-$ in IM occurs through a different mechanism, jump reorientation.[57] Rather than the small angle Gaussian diffusion, the $SeCN^-$ H-bonded to one IM jumps to being H-bonded to another IM with a large angular change. The MD simulations demonstrated the jump reorientation mechanism in IM and provided the value of the average jump angle, 73 ± 5°. Using eq 13, the jump time was calculated to be 17 ps. The overall picture for the reorientation dynamics of $SeCN^-$ in IM is that it initially undergoes inertial motions and consecutive wobbling-in-a-cone, maintaining two H-bonds to the solvent. The longest time scale corresponds to the complete orientational relaxation, which occurs through jump reorientation.

The 2D IR measurements of spectral diffusion report on the solvent structural dynamics. In addition to an ultrafast homogeneous component, the experiments revealed three spectral diffusion time scales (see Table 3). Comparing IM and 1-MeIM at 95 °C, the dynamics in IM is slower, but as with the orientational relaxation, perhaps not as much slower as might be anticipated given the higher viscosity of IM. Like orientational relaxation, the reason lies in the fact that IM has an extensive H-bonding network in contrast to 1-MeIM. The $SeCN^-$'s N lone pair makes H-bonds to two IMs which are embedded in the extended H-bond network (see TOC graphic). As in studies of the OD stretch of HOD in H_2O, where spectral diffusion is caused by the dynamics of the water H-bond network, local fluctuations of the H-bonds on a short time scale and randomization of the network on a longer time scale,[59,60] H-bond dynamics in IM provide a source of spectral diffusion (structural fluctuations) that does not exist in 1-MeIM.

The results from this study explicate the extended hydrogen bond network among IM molecules in the liquid phase and strongly support the presence of hydrogen bonding between IM and $SeCN^-$. Because $SeCN^-$ forms H-bonds with two IM molecules, it inserts into an IM H-bonded chain rather than terminating it. Thus, the $SeCN^-$ anion is a good vibrational probe that can capture the hydrogen bond dynamics of IM.

IM is a very good proton conductor.[8] Like water, proton transport in IM is likely intimately tied to its H-bond network dynamics. Investigations of H-bond dynamics and proton transport in IM and other nonaqueous proton transport liquids can provide further insights into the mechanism of proton mobility.

■ ASSOCIATED CONTENT

Supporting Information

The Supporting Information is available free of charge on the ACS Publications website at DOI: 10.1021/acs.jpcb.8b11299.

Population decay data of deuterated IM, viscosity measurements, calculated orientational correlation functions and angle distributions, first-order Stark effect RISD theory, parallel ($\langle XXXX \rangle$) and perpendicular ($\langle XXYY \rangle$) CLS decay curves with the RISD fits, and fit comparisons of anisotropy and CLS decays (PDF)

(PDF)

■ AUTHOR INFORMATION

Corresponding Author

*Email: fayer@stanford.edu. Phone: (650) 723-4446.

ORCID

Yong-Lei Wang: 0000-0003-3393-7257

Michael D. Fayer: 0000-0002-0021-1815

Present Addresses

‡Department of Materials and Environmental Chemistry, Arrhenius Laboratory, Stockholm University, Stockholm SE-106 91, Sweden (Y.L.W.).

†Institute for Sustainability and Energy at Northwestern, Northwestern University, Evanston, Illinois 60208, United States (J.Y.S.).

Notes

The authors declare no competing financial interest.

■ ACKNOWLEDGMENTS

This work was supported by the National Science Foundation through the CCI program, CHE-1740645 (J.Y.S., principal author). Additional support was provided by the Division of Chemical Sciences, Geosciences, and Biosciences, Office of Basic Energy Sciences of the U.S. Department of Energy through Grant No. DE-FG03-84ER13251 (S.A.Y., S.T.H., and M.D.F.). Y.-L.W. gratefully acknowledges the financial support from the Knut and Alice Wallenberg Foundation. S.A.Y. gratefully acknowledges support from a Stanford Graduate Fellowship. Atomistic molecular dynamics simulations were performed using computational resources (Sherlock Cluster) provided by Stanford University.

■ REFERENCES

(1) Stewart, R. *The Proton: Applications to Organic Chemistry*; Academic Press: Orlando, FL, 1985; Vol. *46*, p 313.

(2) Cain, B. D.; Simoni, R. D. Proton Translocation by the F1F0ATPase of Escherichia Coli. Mutagenic Analysis of the A Subunit. *J. Biol. Chem.* **1989**, *264*, 3292−3300.

(3) Howitt, S. M.; Gibson, F.; Cox, G. B. The Proton Pore of the F0F1-ATPase of Escherichia Coli: Ser-206 Is Not Required for Proton Translocation. *Biochim. Biophys. Acta, Bioenerg.* **1988**, *936*, 74−80.

(4) Lightowlers, R. N.; Howitt, S. M.; Hatch, L.; Gibson, F.; Cox, G. The Proton Pore in the Escherichia Coli F0F1-ATPase: Substitution of Glutamate by Glutamine at Position 219 of the A-Subunit Prevents F0-Mediated Proton Permeability. *Biochim. Biophys. Acta, Bioenerg.* **1988**, *933*, 241−248.

(5) Vik, S. B.; Antonio, B. J. A Mechanism of Proton Translocation by F1F0 ATP Synthases Suggested by Double Mutants of the A Subunit. *J. Biol. Chem.* **1994**, *269*, 30364−30369.

(6) Craven, B. M.; McMullan, R. K.; Bell, J. D.; Freeman, H. C. The Crystal Structure of Imidazole by Neutron Diffraction at 20 °C and −150 °C. *Acta Crystallogr., Sect. B: Struct. Crystallogr. Cryst. Chem.* **1977**, *33*, 2585−2589.

(7) Martinez-Carrera, S. The Crystal Structure of Imidazole at −150 °C. *Acta Cryst.* **1966**, *20*, 783−789.

(8) Kreuer, K. D.; Fuchs, A.; Ise, M.; Spaeth, M.; Maier, J. Imidazole and Pyrazole-Based Proton Conducting Polymers and Liquids. *Electrochim. Acta* **1998**, *43*, 1281−1288.

(9) Hori, Y.; Chikai, T.; Ida, T.; Mizuno, M. Local Structure and Hydrogen Bond Characteristics of Imidazole Molecules for Proton

DOI: 10.1021/acs.jpcb.8b11299
J. Phys. Chem. B 2019, 123, 2094−2105

Conduction in Acid and Base Proton-Conducting Composite Materials. *Phys. Chem. Chem. Phys.* **2018**, *20*, 10311−10318.
(10) Münch, W.; Kreuer, K. D.; Silvestri, W.; Maier, J.; Seifert, G. The Diffusion Mechanism of an Excess Proton in Imidazole Molecule Chains: First Results of an Ab Initio Molecular Dynamics Study. *Solid State Ionics* **2001**, *145*, 437−443.
(11) Scheiner, S.; Yi, M. Proton Transfer Properties of Imidazole. *J. Phys. Chem.* **1996**, *100*, 9235−9241.
(12) Iannuzzi, M.; Parrinello, M. Proton Transfer in Heterocycle Crystals. *Phys. Rev. Lett.* **2004**, *93*, No. 025901.
(13) Iannuzzi, M. Proton Transfer in Imidazole-Based Molecular Crystals. *J. Chem. Phys.* **2006**, *124*, No. 204710.
(14) Chen, H.; Yan, T.; Voth, G. A. A Computer Simulation Model for Proton Transport in Liquid Imidazole. *J. Phys. Chem. A* **2009**, *113*, 4507−4517.
(15) Li, A.; Cao, Z.; Li, Y.; Yan, T.; Shen, P. Structure and Dynamics of Proton Transfer in Liquid Imidazole. A Molecular Dynamics Simulation. *J. Phys. Chem. B* **2012**, *116*, 12793−12800.
(16) Kumar, M.; Venkatnathan, A. Quantum Chemistry Study of Proton Transport in Imidazole Chains. *J. Phys. Chem. B* **2015**, *119*, 3213−3222.
(17) Kawada, A.; McGhie, A. R.; Labes, M. M. Protonic Conductivity in Imidazole Single Crystal. *J. Chem. Phys.* **1970**, *52*, 3121−3125.
(18) Excoffon, P.; Maréchal, Y. H-Bonds of Imidazole Crystals. I. Measurements of Polarized Light IR Spectra. *Chem. Phys.* **1980**, *52*, 237−243.
(19) Wójcik, M. J.; Kwiendacz, J.; Boczar, M.; Boda, Ł.; Ozaki, Y. Quantum-Mechanical and Car−Parrinello Molecular Dynamics Simulations of Infrared Spectra of Crystalline Imidazole. *J. Mol. Struct.* **2014**, *1072*, 2−12.
(20) Flakus, H. R.; Bryk, A. Strong-Coupling Mechanism for Interpretation of the IR Spectra of the Hydrogen Bonded Imidazole Crystal. *J. Mol. Struct.* **1995**, *372*, 215−227.
(21) Wójcik, M. J.; Kwiendacz, J.; Boczar, M.; Boda, Ł.; Ozaki, Y. Theoretical and Spectroscopic Study of Hydrogen Bond Vibrations in Imidazole and Its Deuterated Derivative. *Chem. Phys.* **2010**, *372*, 72−81.
(22) McMullan, R. K.; Epstein, J.; Ruble, J. R.; Craven, B. M. The Crystal Structure of Imidazole at 103 K by Neutron Diffraction. *Acta Crystallogr., Sect. B: Struct. Crystallogr. Cryst. Chem.* **1979**, *35*, 688−691.
(23) Hickman, B. S.; Mascal, M.; Titman, J. J.; Wood, I. G. Protonic Conduction in Imidazole: A Solid-State 15N NMR Study. *J. Am. Chem. Soc.* **1999**, *121*, 11486−11490.
(24) Fischbach, I.; Spiess, H. W.; Saalwächter, K.; Goward, G. R. Solid State NMR Spectroscopic Investigations of Model Compounds for Imidazole-Based Proton Conductors. *J. Phys. Chem. B* **2004**, *108*, 18500−18508.
(25) Ueda, T.; Masui, H.; Nakamura, N. One- and Two-Dimensional 15N Exchange CP/MAS NMR Studies of the Structure and Electronic Properties of the Intermolecular N—H···N Hydrogen Bond in Imidazole Crystal. *Solid State Nucl. Magn. Reson.* **2001**, *20*, 145−155.
(26) Tamimi, A.; Fayer, M. D. Ionic Liquid Dynamics Measured with 2D IR and IR Pump−Probe Experiments on a Linear Anion and the Influence of Potassium Cations. *J. Phys. Chem. B* **2016**, *120*, 5842−5854.
(27) Yamada, S. A.; Bailey, H. E.; Tamimi, A.; Li, C.; Fayer, M. D. Dynamics in a Room Temperature Ionic Liquid from the Cation Perspective: 2D IR Vibrational Echo Spectroscopy. *J. Am. Chem. Soc.* **2017**, *139*, 2408−2420.
(28) Yamada, S. A.; Thompson, W. H.; Fayer, M. D. Water-Anion Hydrogen Bonding Dynamics: Ultrafast IR Experiments and Simulations. *J. Chem. Phys.* **2017**, *146*, No. 234501.
(29) Yuan, R.; Yan, C.; Tamimi, A.; Fayer, M. D. Molecular Anion Hydrogen Bonding Dynamics in Aqueous Solution. *J. Phys. Chem. B* **2015**, *119*, 13407−13415.
(30) Kumar, S. K.; Tamimi, A.; Fayer, M. Comparisons of 2D IR Measured Spectral Diffusion in Rotating Frames Using Pulse Shaping and in the Stationary Frame Using the Standard Method. *J. Chem. Phys.* **2012**, *137*, No. 184201.
(31) Frisch, M. J.; Trucks, G. W.; Schlegel, H. B.; Scuseria, G. E.; Robb, M. A.; Cheeseman, J. R.; Scalmani, G.; Barone, V.; Mennucci, B.; Petersson, G. A.et al. *Gaussian 09*, version D. 01; Gaussian. Inc.: Wallingford CT, 2009.
(32) Wang, Y.-L.; Shah, F. U.; Glavatskih, S.; Antzutkin, O. N.; Laaksonen, A. Atomistic Insight into Orthoborate-Based Ionic Liquids: Force Field Development and Evaluation. *J. Phys. Chem. B* **2014**, *118*, 8711−8723.
(33) Bailey, H. E.; Wang, Y.-L.; Fayer, M. D. The Influence of Hydrophilicity on the Orientational Dynamics and Structures of Imidazolium-Based Ionic Liquid/Water Binary Mixtures. *J. Chem. Phys.* **2018**, *149*, No. 044501.
(34) Dhungana, K. B.; Faria, L. F.; Wu, B.; Liang, M.; Ribeiro, M. C.; Margulis, C. J.; Castner, E. W., Jr. Structure of Cyano-Anion Ionic Liquids: X-ray Scattering and Simulations. *J. Chem. Phys.* **2016**, *145*, No. 024503.
(35) Abraham, M. J.; Murtola, T.; Schulz, R.; Páll, S.; Smith, J. C.; Hess, B.; Lindahl, E. GROMACS: High Performance Molecular Simulations through Multi-Level Parallelism from Laptops to Supercomputers. *SoftwareX* **2015**, *1−2*, 19−25.
(36) Tan, H.-S.; Piletic, I. R.; Fayer, M. D. Polarization Selective Spectroscopy Experiments: Methodology and Pitfalls. *J. Opt. Soc. Am. B* **2005**, *22*, 2009−2017.
(37) Tao, T. Time-Dependent Fluorescence Depolarization and Brownian Rotational Diffusion Coefficients of Macromolecules. *Biopolymers* **1969**, *8*, 609−632.
(38) Tokmakoff, A. Orientational correlation functions and polarization selectivity for nonlinear spectroscopy of isotropic media. I. Third order. *J. Chem. Phys.* **1996**, *105*, 1−12.
(39) Kenkre, V. M.; Tokmakoff, A.; Fayer, M. D. Theory of Vibrational Relaxation of Polyatomic Molecules in Liquids. *J. Chem. Phys.* **1994**, *101*, 10618−10629.
(40) Shin, J. Y.; Yamada, S. A.; Fayer, M. D. Dynamics of a Room Temperature Ionic Liquid in Supported Ionic Liquid Membranes vs. the Bulk Liquid: 2D IR and Polarized IR Pump-Probe Experiments. *J. Am. Chem. Soc.* **2017**, *139*, 311−323.
(41) Kinosita, K., Jr.; Kawato, S.; Ikegami, A. A Theory of Fluorescence Polarization Decay in Membranes. *Biophys. J.* **1977**, *20*, 289−305.
(42) Lipari, G.; Szabo, A. Effect of Librational Motion on Fluorescence Depolarization and Nuclear Magnetic Resonance Relaxation in Macromolecules and Membranes. *Biophys. J.* **1980**, *30*, 489−506.
(43) Lipari, G.; Szabo, A. Model-Free Approach to the Interpretation of Nuclear Magnetic Resonance Relaxation in Macromolecules. 1. Theory and Range of Validity. *J. Am. Chem. Soc.* **1982**, *104*, 4546−4559.
(44) Kramer, P. L.; Giammanco, C. H.; Fayer, M. D. Dynamics of Water, Methanol, and Ethanol in a Room Temperature Ionic Liquid. *J. Chem. Phys.* **2015**, *142*, No. 212408.
(45) Kramer, P. L.; Nishida, J.; Fayer, M. D. Separation of Experimental 2D IR Frequency-Frequency Correlation Functions into Structural and Reorientation-Induced Contributions. *J. Chem. Phys.* **2015**, *143*, No. 124505.
(46) Einstein, A.; Fürth, R. *Investigations on the Theory of Brownian Movement*; Dover Publications: New York, N.Y., 1956.
(47) Moog, R. S.; Ediger, M. D.; Boxer, S. G.; Fayer, M. D. Viscosity Dependence of the Rotational Reorientation of Rhodamine B in Mono- and Polyalcohols. Picosecond Transient Grating Experiments. *J. Phys. Chem.* **1982**, *86*, 4694−4700.
(48) Hu, C.-M.; Zwanzig, R. Rotational friction coefficients for spheroids with the slipping boundary condition. *J. Chem. Phys.* **1974**, *60*, 4354−4357.
(49) Kwak, K.; Park, S.; Finkelstein, I. J.; Fayer, M. D. Frequency-Frequency Correlation Functions and Apodization in Two-Dimen-

DOI: 10.1021/acs.jpcb.8b11299
J. Phys. Chem. B 2019, 123, 2094−2105

sional Infrared Vibrational Echo Spectroscopy: A New Approach. *J. Chem. Phys.* **2007**, *127*, No. 124503.
(50) Kwak, K.; Rosenfeld, D. E.; Fayer, M. D. Taking Apart the Two-Dimensional Infrared Vibrational Echo Spectra: More Information and Elimination of Distortions. *J. Chem. Phys.* **2008**, *128*, No. 204505.
(51) Kramer, P. L.; Nishida, J.; Giammanco, C. H.; Tamimi, A.; Fayer, M. D. Observation and Theory of Reorientation-Induced Spectral Diffusion in Polarization-Selective 2D IR Spectroscopy. *J. Chem. Phys.* **2015**, *142*, No. 184505.
(52) Giammanco, C. H.; Kramer, P. L.; Yamada, S. A.; Nishida, J.; Tamimi, A.; Fayer, M. D. Carbon dioxide in an ionic liquid: Structural and rotational dynamics. *J. Chem. Phys.* **2016**, *144*, No. 104506.
(53) Padró, J. A.; Saiz, L.; Guardia, E. Hydrogen bonding in liquid alcohols: a computer simulation study. *J. Mol. Struct.* **1997**, *416*, 243−248.
(54) Tavernier, H. L.; Fayer, M. D. Solute-Solute Spatial Distribution in Hydrogen Bonding Liquids Probed with Time-dependent Intermolecular Electron Transfer. *J. Chem. Phys.* **2001**, *114*, 4552−4564.
(55) Tamimi, A.; Bailey, H. E.; Fayer, M. D. Alkyl Chain Length Dependence of the Dynamics and Structure in the Ionic Regions of Room-Temperature Ionic Liquids. *J. Phys. Chem. B* **2016**, *120*, 7488−7501.
(56) Tamimi, A.; Fayer, M. D. Ionic Liquid Dynamics Measured with 2D IR and IR Pump−Probe Experiments on a Linear Anion and the Influence of Potassium Cations. *J. Phys. Chem. B* **2016**, *120*, 5842−5854.
(57) Laage, D.; Hynes, J. T. A Molecular Jump Mechanism of Water Reorientation. *Science* **2006**, *311*, 832−835.
(58) Fecko, C. J.; Loparo, J. J.; Roberts, S. T.; Tokmakoff, A. Local Hydrogen Bonding Dynamics and Collective Reorganization in Water: Ultrafast Infrared Spectroscopy of HOD/D_2O. *J. Chem. Phys.* **2005**, *122*, No. 054506.
(59) Asbury, J. B.; Steinel, T.; Stromberg, C.; Corcelli, S. A.; Lawrence, C. P.; Skinner, J. L.; Fayer, M. D. Water Dynamics: Vibrational Echo Correlation Spectroscopy and Comparison to Molecular Dynamics Simulations. *J. Phys. Chem. A* **2004**, *108*, 1107−1119.
(60) Park, S.; Fayer, M. D. Hydrogen Bond Dynamics in Aqueous NaBr Solutions. *Proc. Natl. Acad. Sci. U.S.A.* **2007**, *104*, 16731−16738.

DOI: 10.1021/acs.jpcb.8b11299
J. Phys. Chem. B 2019, 123, 2094−2105